Proceedings of ASME Turbo Expo 2020
Turbomachinery Technical Conference and Exposition
GT2020
June 22-26, 2020, London, England

GT2020-14665

ANALYSIS OF THERMOACOUSTIC MODES IN CAN-ANNULAR COMBUSTORS USING EFFECTIVE BLOCH-TYPE BOUNDARY CONDITIONS

Jakob G. R. von Saldern[a], **Alessandro Orchini**[a] **and Jonas P. Moeck**[*b]
[a]Chair of Fluid Dynamics, Technische Universität Berlin, Berlin, Germany
[b]Department of Energy and Process Engineering, Norwegian University of Science and Technology, Trondheim, Norway

ABSTRACT

Heavy-duty gas turbines are commonly designed with can-annular combustors, in which all flames are physically separated. Acoustically, however, the cans communicate via the upstream located compressor plenum, or at the downstream gaps found at the transition to the turbine inlet. In the present study, a coupling condition that is based on a Rayleigh conductivity and acoustic flux conservation is derived. It enables acoustic communication between adjacent cans, in which one-dimensional acoustic waves propagate. In addition, because can-annular systems commonly feature a discrete rotational symmetry, the acoustic field can be expressed as a Bloch-periodic wave in the azimuthal direction. We demonstrate how the coupling conditions resulting in a combustion system with N cans can be expressed as an effective impedance for a single can. By means of this Bloch-type boundary condition, the thermoacoustics of a can-annular system can be analyzed considering only one can, thus reducing the size of the problem by a factor of N. Using this method, we investigate in frequency domain the effect of the coupling strength of a generic can-annular combustor consisting of 12 identical cans, which are connected at the downstream end. We describe generic features of can-annular systems that can be efficiently addressed with this framework and derive results on the frequency response of the cans at various Bloch numbers in the low-frequency and high-frequency limits. Furthermore, the formation of eigenvalue clusters with eigenvalues of close frequency and growth rate, but very different mode shapes is discussed.

[*]Address all correspondence to this author, jonas.moeck@ntnu.no.

NOMENCLATURE

Roman

A_c	cross sectional can area
A_g	gap area
b	Bloch wavenumber/azimuthal mode order
c	speed of sound
f	downstream propagating acoustic wave amplitude
g	upstream propagating acoustic wave amplitude
i	imaginary unit
j,l	index for can number
k	distance between cans
m	acoustic–flame coupling strength
$\mathbf{M}_b$	acoustic system matrix
$\widetilde{\mathbf{M}}_b$	thermoacoustic system matrix
N	number of cans
$\hat{p}$	Fourier transform of acoustic pressure
$\hat{q}$	Fourier transform of heat release rate fluctuation
r_c	can radius
r_g	gap radius
R_b	effective reflection coefficient
R_{gas}	gas constant
R_1	upstream reflection coefficient
R_2	downstream reflection coefficient
s	Laplace variable
t	time
T_j	transmission coefficient
$\hat{u}$	Fourier transform of acoustic velocity
x	axial coordinate
Z_b	effective impedance

Greek

α	gap-to-can radii ratio
γ	specific heat ratio
θ_j	discrete azimuthal coordinate
ρ	density
σ	growth rate
τ	time lag
ψ_b	axial pressure mode shape at Bloch number b
ω	angular frequency

Abbreviations

FTF	Flame transfer function

Introduction

Can-annular combustors are commonly installed in modern heavy-duty gas turbines. They consist of a set of nominally identical cans aligned next to each other along a ring, whose center is the axis of the turbine rotor. At the upstream end, all the cans are connected to the compressor plenum. Downstream, the cans end into the turbine. Since in each can a flame burns in an essentially isolated manner, can-annular combustors have often been approximated by isolated single can systems when investigating thermoacoustic stability. Acoustic communication between adjacent cans has been neglected. Recent studies, however, have shown that the acoustic can-to-can communication that arises via the compressor plenum or connection gaps before the first turbine stage cannot be neglected even if the connection points are small.

Acoustic interaction between adjacent cans was first numerically and experimentally examined in [1]. By comparing thermoacoustic oscillations in a single can with the oscillations in a quarter of a 16 can combustor, the study revealed that can-to-can communication is not negligible. Experimental evidence of acoustic interaction between adjacent cans was also presented in [2], in conjunction with a modal analysis of the acoustics of a simplified two dimensional can-annular configuration with 8 cans. Acoustic mode shapes that involve multiple cans, and thus cannot be found by examining a single isolated can only, were observed. The effect of the cross-talk gap between adjacent cans at the turbine inlet on the acoustic cross-talk between the cans was numerically examined in [3]. In [4], it was theoretically discussed how azimuthal modes can arise in can-annular combustors even for a weak acoustic can-to-can coupling. Numerical results based on the two-dimensional Helmholtz equation showed that weak acoustic coupling causes the formation of eigenvalue clusters, in which a group of N eigenvalues have closely spaced frequencies. The results were validated with experimental data of a 12 can combustor, in which modes of different azimuthal order, oscillating at close frequencies were observed. Moreover, Bloch-periodic boundary conditions, which exploit the discrete rotational symmetry of the system, were applied to a single can, thereby reducing the dimension of numerical models by the degree of symmetry. Only recently, experimental studies on thermoacoustics in a two-can combustor model with a downstream coupling through a cross-talk tube aligned normal to the flow direction were conducted [5, 6]. Depending on the equivalence ratio and geometric boundary conditions, push–push (in phase), push–pull (in anti-phase) and bi-modal oscillation patterns with close frequencies were observed.

Although thermoacoustic phenomena in axial and annular combustor geometries have been studied extensively, thermoacoustics in can-annular combustors have received much less attention. Below the cut-on frequency of transverse modes, acoustic waves in ducts are of axial form. Single can combustors are often regarded as ducts, for which low-order thermoacoustic network models, based on plane axial waves, are well established [7]. In the present study, an extension of this type of single can combustor low-order models to a generic can-annular combustor model is presented. The acoustics inside each can remain one dimensional, whereby an acoustic can-to-can communication is enabled by a coupling boundary condition. This condition is based on the Rayleigh conductivity and acoustic flux conservation. By exploiting the discrete rotational symmetry, the coupling boundary condition is also expressed as a novel effective Bloch-type boundary condition. When applied at the boundary of a single can, this effective boundary condition models the corresponding response of a can-annular combustor with N identical cans. The equations to analyze the thermoacoustic stability of a generic can-annular combustor are presented, explicit expressions for transmission of acoustics across cans are derived, and the effect of coupling strength on acoustic and thermoacoustic modes of a can-annular configuration with 12 cans is investigated. The presented generic can-annular combustor model is based on the weak coupling between the 1D acoustics in each can using the Bloch ansatz. It therefore significantly differs from other low-order modeling approaches, which model azimuthal and axial acoustic waves in fully annular geometries, such as the one presented in [8].

Acoustic coupling boundary condition

We consider a generic can-annular combustor consisting of N nominally identical cans and assume one-dimensional acoustic wave propagation in each of the cans. The cans are considered to be acoustically closed ($\hat{u} = 0$) downstream, to emulate the choked boundary condition of the combustor outlet. However, a small aperture at the downstream end, at $x = l_2$, allows for acoustic communication between adjacent cans (see Figure 1). Mass flux conservation at the downstream end in can j yields

$$\hat{u}_j A_c + \hat{u}_{j-1,j} A_g - \hat{u}_{j,j+1} A_g = 0 \quad \text{at } x = l_2, \tag{1}$$

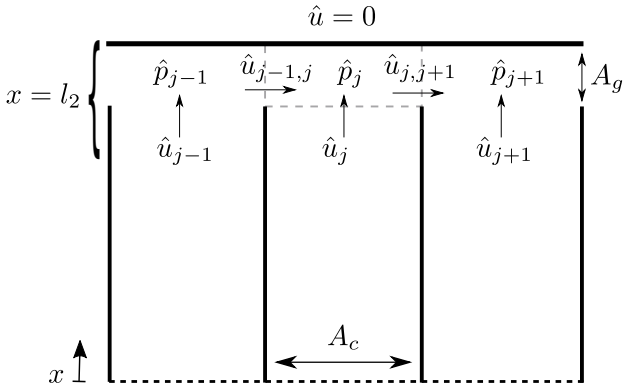

FIGURE 1: Sketch of a generic can-annular arrangement with connection points of adjacent cans indicated.

where $\hat{u}_j$ denotes the Fourier transform of the acoustic velocity in can j, $\hat{u}_{j,j+1}$ the acoustic velocity in the connection gap between cans j and $j+1$, A_c is the cross sectional can area, and $A_g = \pi r^2$ is the connection gap area. The acoustic flux conservation is evaluated at $x = l_2$ although the connection gaps have a spatial extension in the x direction. This implies that the equation is an approximation valid only for acoustically compact gaps. Since the acoustic wave propagation is assumed to be one dimensional, the acoustic fluctuations inside the gaps are related to the acoustic fluctuations in the axial direction by the Rayleigh conductivity [9, 10]

$$K_R \equiv -\frac{s\hat{u}_{j,j+1}\rho A_g}{\hat{p}_{j+1}-\hat{p}_j} \quad \text{at } x = l_2, \tag{2}$$

where ρ is the gas density and $\hat{p}$ is the Fourier transform of the acoustic pressure. The strength of the coupling is determined by the Rayleigh conductivity K_R, which we model using known results. Complex models of the Rayleigh conductivity can be found in the literature. For example, a frequency dependent model that also includes mean flow effects inside the gaps was presented in [11]; the effect of a tangential mean flow on the Rayleigh conductivity was discussed for different gap geometries in [12, 13]. Nonetheless, in this study we use a simple constant model for the Rayleigh conductivity. By assuming circular gaps and by neglecting wall thickness and mean flow effects, the Rayleigh conductivity scales with the gap radius, $K_R = 2r_g$ [11].

Solving Eq. (2) for the velocity amplitudes in the gaps and inserting the latter in Eq. (1) yields a downstream coupling boundary condition:

$$\hat{u}_j A_c - \frac{2r_g}{s\rho}(2\hat{p}_j - \hat{p}_{j-1} - \hat{p}_{j+1}) = 0 \quad \text{at } x = l_2. \tag{3}$$

Equation (3) serves as a coupling boundary condition that allows the one-dimensional acoustics of adjacent resonators to communicate. Note that in the limit in which no communication is allowed between the cans, $r_g = 0$, we retrieve from Eq. (3) $\hat{u}_j = 0$, as expected for a closed (sound hard) can termination. In order to model the acoustics of a generic can-annular combustor with acoustic coupling between the cans, Eq. (3) must be applied at the downstream boundary of each can.

Effective Bloch-type boundary condition

Due to the discrete rotational symmetry of the generic can-annular combustor, the coupling boundary condition (3) can be expressed in form of an effective Bloch-periodic boundary condition. In a can-annular system with discrete rotational symmetry, in which the can-acoustics are one dimensional, the acoustic pressure can be written as a Bloch wave [4, 14, 15]

$$\hat{p}(x,\theta_j) = \sum_b \hat{p}_{j,b}(x) = \sum_b \psi_b(x) e^{-ib\theta_j}, \tag{4}$$

where b is the Bloch wavenumber, $\theta_j \equiv (j-1)2\pi/N$ is the discrete coordinate in the azimuthal direction, and ψ_b is the axial acoustic pressure for a given Bloch wavenumber. Since the acoustics within the cans are assumed to be one dimensional, the Bloch wavenumber coincides with the azimuthal order of the acoustic wave. Consequently, ψ_b is identical in each can and only depends on the axial coordinate. For a generic can-annular combustor with N cans, the Bloch wavenumber takes values $b = [0, \pm 1, \ldots, \pm(N/2-1), N/2]$ or $b = [0, \pm 1, \ldots, \pm(N-1)/2]$ for even or odd values of N, respectively. The Bloch wave approach allows to relate the acoustic pressure in can $j+1$ to the acoustic pressure in can j for any given b, by means of a phase shift

$$\hat{p}_{j+1,b}(x) = \hat{p}_{j,b}(x) e^{-ib\frac{2\pi}{N}} \quad \forall b. \tag{5}$$

Accordingly, the pressure in can $j-1$ can be expressed with the pressure in can j and a phase shift in the opposite direction. Inserting this ansatz into Eq. (3) yields an effective Bloch-type impedance:

$$Z_b(s) \equiv \frac{\hat{p}_{j,b}}{\hat{u}_{j,b}} = \frac{s\rho A_c}{8 r_g \sin^2\left(\frac{\pi b}{N}\right)}, \quad \text{at } x = l_2. \tag{6}$$

If this effective Bloch-type impedance is applied at the downstream boundary of a single can, the resulting system models the response of a can-annular system with N identical cans for a given Bloch wavenumber.

The Bloch wave formulation, Eq. (5), also allows for an interpretation of possible mode shapes [4]. For $b = 0$ all cans oscillate in phase and the mode is called a push–push mode. For

$b = N/2$ (even N only), adjacent cans oscillate in anti-phase and the mode is called a push–pull mode. For all other values of $\pm b$, the two mode shapes correspond to two counter-rotating waves with azimuthal order b, and are associated with degenerate eigenvalues; they can, hence, be combined to represent azimuthally standing waves.

Generic can-annular combustor model

In this section, the effective Bloch-type boundary condition (6) is applied at the downstream boundary of a single can to derive a low-order thermoacoustic model of a generic can-annular combustor consisting of N identical cans. Parameters will be chosen to analyze a generic can-annular combustor model, without the aim of reproducing a specific configuration.

We consider a can with a total length of 1 m and a compact heat source at $x = 0$, as sketched in Figure 2. The heat source separates the can in an upstream (subscript 1) and a downstream (subscript 2) region. The temperature is set to $T_1 = 300$ K in the upstream region and increases by a factor of two across the flame. The mean flow is assumed to be zero; thus, the mean pressure $\bar{p} = 1$ bar does not change across the flame zone. The densities in the two regions are assumed to follow the ideal gas law, with gas constant $R_{\text{gas}} = 287$ J/(kg K). The mean heat release, $\bar{q}$, can be computed by imposing energy conservation. By assuming only plane acoustic waves, the acoustic pressure and acoustic velocity inside each of the two regions read [16, 17]

$$p'(x,t) = \hat{p}(x)e^{st} = (fe^{-\frac{xs}{c}} + ge^{+\frac{xs}{c}})e^{st}, \tag{7}$$

$$u'(x,t) = \hat{u}(x)e^{st} = \frac{1}{\rho c}(fe^{-\frac{xs}{c}} - ge^{+\frac{xs}{c}})e^{st}, \tag{8}$$

where $c \equiv \sqrt{\gamma R_{\text{gas}} T}$ denotes the speed of sound, $s \equiv \sigma + i\omega$ is the complex frequency, and g and f are the amplitudes of the up- and downstream traveling acoustic waves, respectively. The ratio of specific heats is set to $\gamma = 1.4$. To relate the acoustic fluctuations across the flame element, the Rankine–Hugoniot jump conditions are invoked at $x = 0$ [17, 18]

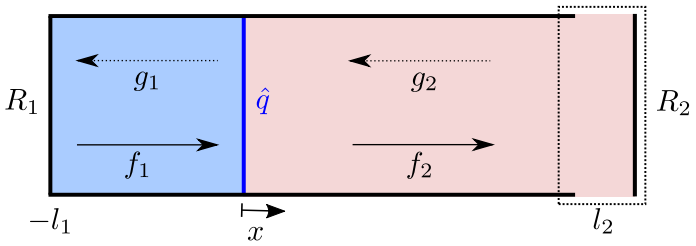

FIGURE 2: Plane acoustic waves in a single can with compact heat source. The downstream boundary condition models the response of a corresponding can-annular system.

$$\hat{p}_2 - \hat{p}_1 = 0, \tag{9a}$$

$$\hat{u}_2 - \hat{u}_1 = \frac{\gamma - 1}{\rho_1 c_1^2 A_c}\hat{q}, \tag{9b}$$

where $\hat{q}$ is the Fourier transform of the compact heat release rate fluctuation, and the radius of the cross-sectional can area is set to $r_c = 0.05$ m. For this choice of parameters the cut-on frequency of transversal modes is above 1000 Hz. As we consider $r_g < r_c$, the compactness assumption of the gaps is fulfilled in this frequency range. To model an acoustic can-to-can communication, the Bloch-type boundary condition is applied at the downstream end. The effective impedance, Eq. (6), can be expressed in form of an effective reflection coefficient $R \equiv g/f$; it reads:

$$R_b(s) = \frac{Z_b - \rho c}{Z_b + \rho c} = 1 - \frac{16 r_g c_2 \sin^2\left(\frac{\pi b}{N}\right)}{s A_c + 8 r_g c_2 \sin^2\left(\frac{\pi b}{N}\right)} \tag{10}$$

The effective reflection condition is applied at the downstream boundary of the single can, $R_2 = R_b$. It transforms the axial model into a can-annular model.

The upstream reflection coefficient, at $x = -l_1 = -0.2$ m, is set to $R_1 = 0.95$ to introduce some damping. The upstream boundary condition could be chosen to a Bloch-type coupling boundary condition in an analogous manner. However, in this study we assume acoustic coupling only at the downstream end. The two boundary conditions and the jump conditions yield:

$$\underbrace{\begin{bmatrix} -R_1 e^{-\tau_1 s} & 1 & 0 & 0 \\ 1 & 1 & -1 & -1 \\ 1 & -1 & -\frac{\rho_1 c_1}{\rho_2 c_2} & \frac{\rho_1 c_1}{\rho_2 c_2} \\ 0 & 0 & 1 & -R_b(s) e^{-\tau_2 s} \end{bmatrix}}_{\mathbf{M}_b(s)} \underbrace{\begin{bmatrix} g_1 \\ f_1 \\ g_2 \\ f_2 \end{bmatrix}}_{\mathbf{g}} = \begin{bmatrix} 0 \\ 0 \\ \frac{\hat{q}}{c_1 A_c} \\ 0 \end{bmatrix}, \tag{11}$$

where the time lags are defined as $\tau_1 \equiv 2l_1/c_1$ and $\tau_2 \equiv 2l_2/c_2$.

For $\hat{q} = 0$, Eq. (11) can be solved for the acoustic eigenvalues. In order to solve for thermoacoustic eigenvalues, the heat release rate fluctuation needs to be related to the acoustic fluctuations; this is achieved by introducing the Flame Transfer Function (FTF):

$$\text{FTF} \equiv \frac{\hat{q}}{\bar{q}} \frac{\bar{u}}{\hat{u}} \tag{12}$$

We extract the FTF from forced simulations of the well-established kinematic G-equation representation of a laminar

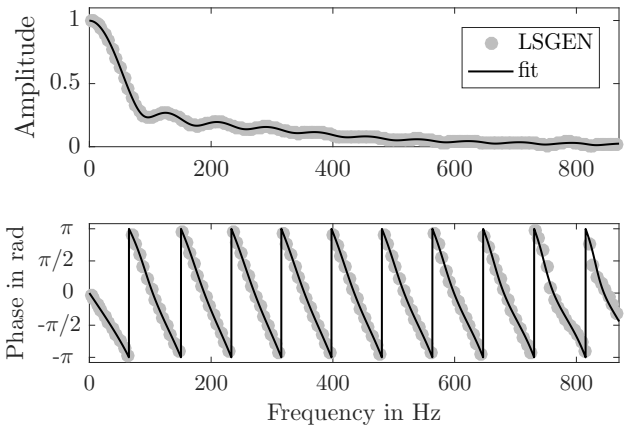

FIGURE 3: Flame Transfer Function of a conical laminar premixed flame extracted from LSGEN (markers) and fitted onto a continuous state-space model (solid line).

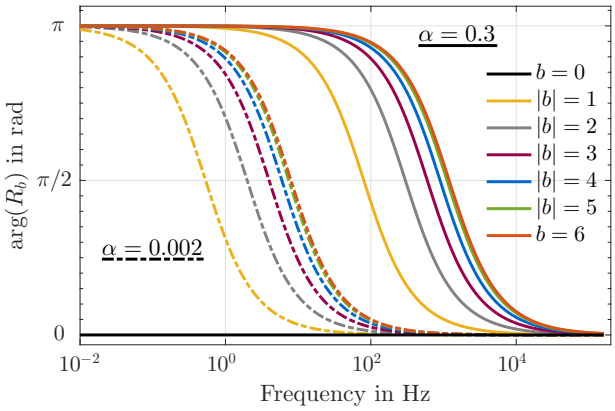

FIGURE 4: Phase of the effective reflection coefficient for $\alpha = 0.002$ and $\alpha = 0.3$ and different Bloch wavenumbers as a function of frequency.

conical flame [19, 20, 21], with a radius of 5.5 mm and a length of 16.5 mm. The LSGEN code, which uses a level set method to solve the G-equation, is used to determine the FTF for the present study. The code has been thoroughly validated and used to extract the FTFs of two dimensional slot laminar flames [22], rotationally symmetric conical flames [23], and more complex turbulent partially premixed flames [24]. Figure 3 shows the FTF for a range of frequencies (gray dots) for an acoustic forcing with 1% of the mean flow velocity, which is set to 1.5 m/s. A rational transfer function is fitted to the data (black line) using a pole relocation method based on the algorithm presented in [25].

When the FTF is introduced in Eq. (11), an eigenvalue problem of the form

$$\widetilde{\mathbf{M}}_b(s)\mathbf{g} = \mathbf{0} \tag{13}$$

arises, which can be solved for the thermoacoustic eigenvalues s. Note that the downstream reflection coefficient depends on the Bloch wavenumber and therefore Eq. (13) has to be solved for each possible azimuthal order b. However, by applying the effective reflection coefficient to a single can, the size of the eigenvalue problem is reduced by the degree of symmetry, compared to the eigenproblem that arises when considering the acoustics in the full system with N cans. Solving N reduced eigenvalue problems is numerically more efficient and robust than solving one problem which is N times larger in size.

Effective reflection and transmission coefficient

The effective reflection coefficient $R_b(s)$ is frequency and Bloch wavenumber dependent. Figure 4 shows the phases of the frequency responses ($\sigma = 0$) of $R_b(i\omega)$ for all Bloch wavenumbers of a 12-can configuration and two different gap radii. We indicate the ratio of the gap radius and the can radius with $\alpha \equiv r_g/r_c$. Since no acoustic losses are accounted for at the downstream end, the absolute values of the effective reflection coefficients are 1 for all frequencies and Bloch wavenumbers, $|R_b(i\omega)| = 1$. Due to the $\sin^2()$ function, the responses for negative and positive Bloch wavenumbers are identical. For $b = 0$ the reflection coefficient is 1 for all frequencies and represents a sound hard boundary condition. For $b \neq 0$ the reflection coefficient is -1 ($\arg(R_b) \to \pi$) for low frequencies and converges to 1 ($\arg(R_b) \to 0$) for large frequencies. Hence, at large frequencies the effective reflection coefficient behaves as a closed-end boundary condition for all b. Larger values of the gap radius shift the transition from open to closed-end boundary condition to higher frequencies.

The effective reflection coefficient can also be used to analyze how acoustic waves are transmitted into adjacent cans. The acoustic wave at the downstream boundary in can l is transmitted into can j by the transmission coefficient T_{j-l}. Note that T_0 is a reflection coefficient, but will still be denoted with the symbol T_0 in the following. Due to the discrete rotational symmetry the transmission coefficient only depends on the distance between the two cans and can be computed by summing over all possible Bloch wavenumbers at a given frequency:

$$T_{j-l}(s) = \frac{1}{N}\sum_b R_b(s) e^{-ib(\theta_j - \theta_l)}. \tag{14}$$

The Bloch phase shift determines the distance to the forcing, Eq. (5). Figure 5 shows the absolute values and phases of the transmission coefficient T_k, where $k = j - l$ denotes the distance

between the cans. The total can number is set to $N = 12$ and the connection gap radius to 5% of the can radius ($\alpha = 5\%$). The maximum distance between two cans in this configuration is 6 cans. In [4], transmission coefficients of a two dimensional can-annular model with the same can number were presented. The study in [4] looks at the transmission from an upstream traveling wave at $x = 0$ in can l to the downstream traveling wave at $x = 0$ in can j, and thus includes part of the acoustic response of the can. In order to model the same transmission, the transmission coefficients we present in Eq. (14) should be multiplied by $\exp(-\tau_2 s)$. However, we decide to focus only on the transmission coefficient at the can end (at $x = l_2$). Taking can-acoustic effects into account leads to an additional phase drop which is can dependent and makes it more challenging to interpret the pure contribution of can-to-can coupling effects on the system. Figure 5 shows that the transmission to closer cans is stronger. In the zero-frequency limit, the gain of reflection coefficient T_0 tends to $1-2/N$, whereas the gains for all other transmission coefficients, T_k for $k \neq 0$, tend to $2/N$. This behavior was also reported in [4], Fig. 9, but no explantion was given. With the effective reflection coefficient, Eq. (10), and the formula for the transmission coefficient for adjacent cans, Eq. (14), it can be proven that this is the case for every N:

$$\lim_{i\omega\to 0}|T_k| = 1-\frac{2}{N},\ k=0 \qquad \lim_{i\omega\to 0}|T_k| = \frac{2}{N},\ k\neq 0. \tag{15}$$

The first relation can also be directly observed in Figure 4. For $b = 0$ the effective reflection coefficient at $\omega = 0$ is 1, for all other $N-1$ Bloch wavenumbers, the effective reflection coefficients are -1. Averaging these values yields the result shown in Eq. (15). The proof of the second relation for $k \neq 0$ can be found in Appendix A.

At higher frequencies, there are some differences between our results shown in Figure 5 and those reported in [4]. In Figure 5 the gain of the T_0 reflection coefficient converges to 1, all other transmission coefficients converge to 0, which means that the acoustic wave remains confined in the first can. This is consistent with the results shown in Figure 4; at high frequencies the effective reflection coefficient converges to 1 for all b. The model in [4], however, is two dimensional and resolves the gap size in axial direction, whereas in the present study the reflection coefficient is just applied at one x location and thus can only be used when the axial extent of the gap is small. The study in [4] uses a larger gap radius and could therefore represent effects that cannot be resolved with the model presented here, even if a larger gap radius would be used. A more complex model of the Rayleigh conductivity could compensate for these effects, but is not considered in the present study. The phases shown in [4] for the transmission coefficients include can-acoustic wave propagation. It has been verified (not shown) that they qualitatively agree well with the phase of the transmission coefficients of the

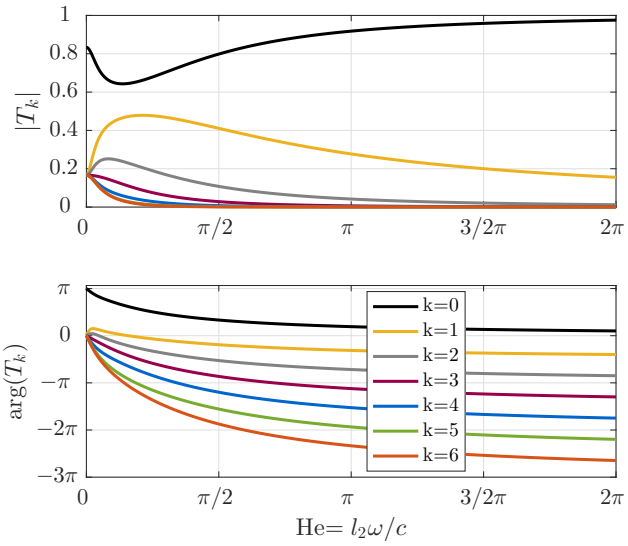

FIGURE 5: Amplitudes and phases of transmitted waves to cans of different distances ($k = 0 \ldots N/2$) for $\alpha = 5\%$ as a function of the Helmholtz number.

present study if can-acoustic effects are included in this model as well. At $\omega = 0$ the $k = 0$ phase starts from π, for $k \neq 0$ the phases start from 0. For high frequencies, the acoustic wave is not reflected into the adjacent cans. It is, however, interesting to note that the phases of the transmission coefficients converge to constant values, equispaced at multiples of $\pi/2$, which can also be observed for any value N, even or odd.

The transmission coefficients do not contain any damping elements. Consequently, the acoustic fluctuation energy must be conserved, and the sum of all magnitude-squared transmission coefficients must be 1 at any given frequency:

$$\sum_{k=-5}^{6}|T_k|^2 = 1 \tag{16}$$

It can also be shown that the sum of the transmission coefficients equals unity:

$$\begin{aligned}\sum_k T_k &= \sum_k \frac{1}{N}\sum_b R_b(s)e^{-ib\theta_k}\ldots \\ &= \frac{1}{N}\sum_b R_b(s)\sum_k e^{-ibk2\pi/N} = 1,\end{aligned} \tag{17}$$

with $\theta_k \equiv 2\pi k/N$. The sum over k equals 0 for every $b \neq 0$, and equals N for $b = 0$. The reflection coefficient is 1 for $b = 0$ and independent of frequency (see Figure 4).

Note that the results presented in Eqs. (15)-(17) are independent of α. The transmission coefficients results shown in Figure 5 for $\alpha = 5\%$ are qualitatively the same for other values of α, and have exactly the same limits at $\omega \to 0$ and $\omega \to \infty$. The high-frequency limits are reached quicker for smaller values of α. This can be seen in Figure 4: for smaller values of α, the reflection coefficient converges to the closed end limit at lower frequencies.

Can-annular acoustics

The generic can-annular combustor is first analyzed from a pure acoustics point of view (Eq. (11) with $\hat{q} = 0$). The acoustic eigenvalues s_A are solutions of $\det[\mathbf{M}_b(s_A)] = 0$ and are obtained using root-finding algorithms. Figure 6 shows the acoustic eigenvalues of the generic can-annular combustor with $N = 12$ cans and $\alpha = 20\%$ between 0 and 1250 Hz. Eigenvalues have also been computed in a full-setup, i.e., without the use of the Bloch boundary condition (10) but with the coupling condition (3) applied to all N cans. The resulting eigenvalues are indicated with black dots in Figure 6, and validate the cheaper calculations performed with the Bloch formalism. Figure 6 shows that the acoustic eigenvalues form clusters, in the sense that groups of eigenvalues are close in frequency and growth rate. Each cluster contains N eigenvalues, one for each Bloch wavenumber b. Given the symmetries of the configuration, most of these are two-fold degenerate. In particular only the eigenvalues found for $b = 0$ (and $b = N/2$ if N is even) are not degenerate. Moreover, it can be observed that for increasing Bloch wavenumbers within one cluster, the corresponding acoustic eigenvalues show higher frequencies; the $b = 0$ acoustic eigenvalue is always the eigenvalue

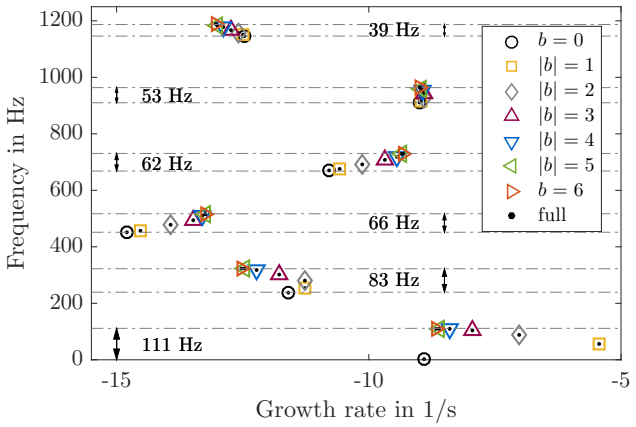

FIGURE 6: Acoustic eigenvalues for a can-annular combustor with $N = 12$ cans and $\alpha = 20\%$. The symbols indicate the Bloch wavenumber, the dots inside the symbols are solutions of the full system without Bloch-type boundary condition.

with the lowest frequency, the $b = 6$ the one with the highest frequency. For increasing frequencies, the clusters become more dense, i.e., the eigenvalues move even closer. This results from the effective reflection coefficient, which, as shown in Figure 4, converges to 1 (sound hard) for every b at high frequencies. In the limit $\omega \to \infty$ the cans become decoupled and show 12 times the same eigenvalue. However, this is a theoretical consideration since the gaps are assumed to be acoustically compact, an assumption that breaks down at very large frequencies.

It is interesting to note that for $b = 0$, the effective reflection coefficient is 1, and the acoustic matrix $\mathbf{M}_0$ is not dependent on the coupling strength r_g nor on the total can number N. Accordingly, the same acoustic eigenvalues for $b = 0$ shown in Figure 6 exist for any value of α and N. This results from the fact that the $b = 0$ eigenvalue corresponds to a push–push mode, which also exist in a single can. For an even number of cans, the $b = N/2$ eigenvalues always show the same values, too. They correspond to a push–pull mode, which already exists in a system composed of only two cans. However, the $b = N/2$ eigenvalues are affected by the gap radius. These findings also hold for the thermoacoustic system, discussed next.

Effect of coupling strength on acoustic and thermoacoustic eigenvalues

The small size of the low-order generic can-annular combustor model, Eq. (11), allows for extensive parametric studies at low computational cost. In the following, the effect of acoustic coupling strength between the cans is investigated by varying the gap size. Thermoacoustic eigenvalues s_T solve Eq. (13) and can be found in a manner analogous to the purely acoustic case. Figure 7 shows the acoustic and thermoacoustic eigenvalues of the 12-can combustor for a cluster of eigenvalues between 230 and 290 Hz (left) and one between 445 and 485 Hz (right). We set the coupling parameter α to 5%. The symbols indicate the Bloch wavenumber. The colored lines show the paths along which all eigenvalues move when the gap radius is decreased ($\alpha \to 0$). The color indicates the α values at the positions of the $b = 6$ eigenvalues. In order to track the mapping between acoustic and thermoacoustic eigenvalues, when the acoustics are coupled with the flame, an artificial parameter m is introduced before the heat release term in Eq. (11), $\hat{q}_{\text{new}} = m\hat{q}$. The dotted lines show the trajectories of the thermoacoustic eigenvalues when m is varied from $m = 1$ (full coupling) to $m = 0$ (no coupling). As the acoustic–flame coupling is reduced $m \to 0$, the thermoacoustic eigenvalues converge to acoustic eigenvalues with the same Bloch wavenumber. The acoustic–flame coupling shifts the thermoacoustic eigenvalues mostly in growth rate and only to a lesser extent in frequency. Note that the parameter m is non-physical and only used to demonstrate the effect of acoustic–flame coupling.

All acoustic and thermoacoustic eigenvalues move along the

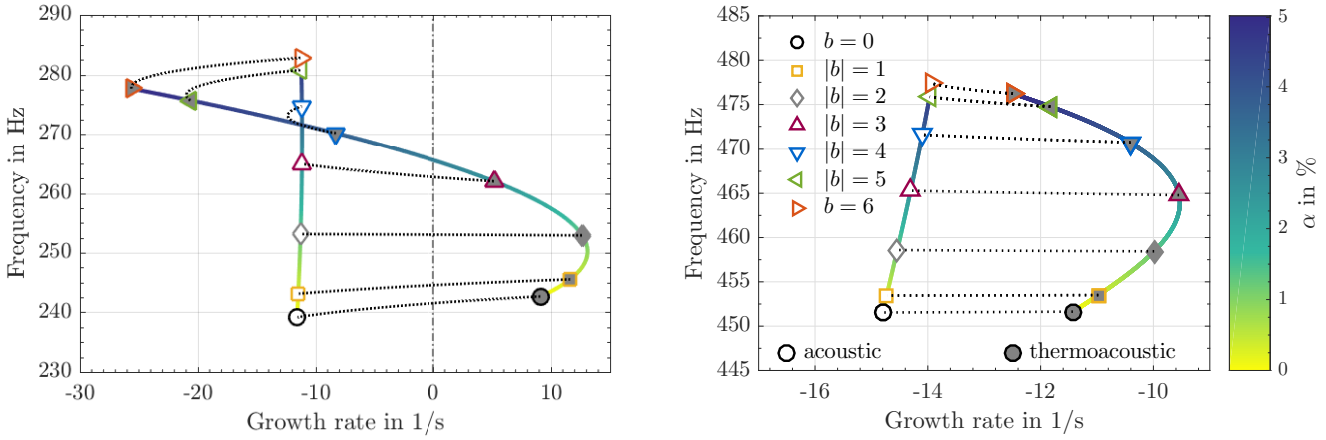

FIGURE 7: Acoustic and thermoacoustic eigenvalues of the generic can-annular combustor with 12 cans and $\alpha = 5\%$. The left figure shows a cluster between 230 and 290 Hz and the right figure a cluster between 445 and 485 Hz. The colored lines show the paths along which the eigenvalues move for a varying gap radius. The color indicates α values at the positions of the $b = 6$ eigenvalues. The dotted lines show the paths along which the thermoacoustic eigenvalues move if the acoustic–flame coupling is continuously decreased.

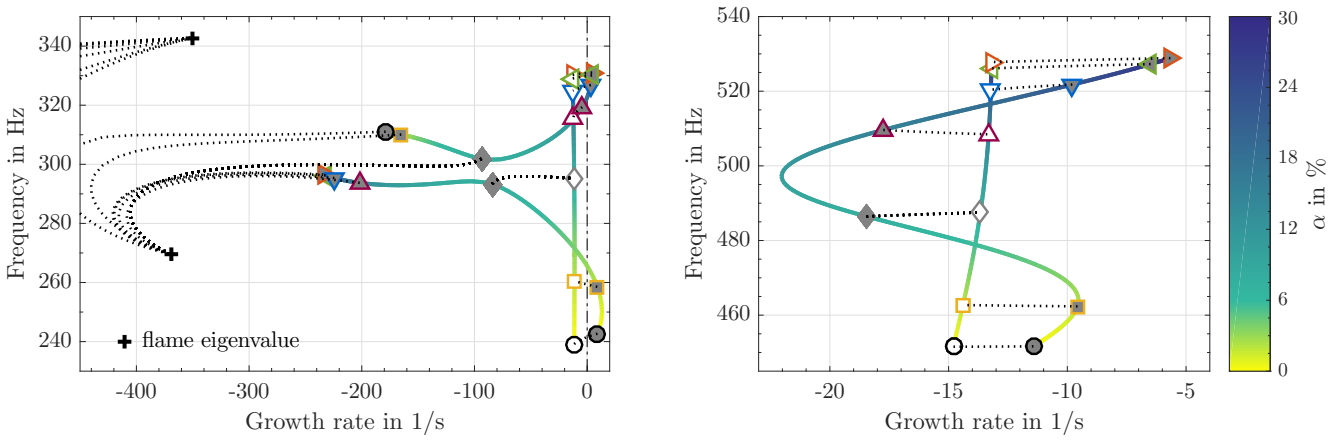

FIGURE 8: Acoustic and thermoacoustic eigenvalues of the generic can-annular combustor with 12 cans and $\alpha = 30\%$. The left figure shows eigenvalues between 230 and 350 Hz and the right figure eigenvalues between 445 and 540 Hz. Symbols and lines are as in Figure 7, the black crosses denote flame eigenvalues.

same paths, as the radius is varied, but at different rates depending on the Bloch wavenumber. The acoustic eigenvalues have similar growth rates and vary mostly in frequency, the thermoacoustic eigenvalues, instead, show a strong shift in growth rate, which results from the frequency dependent acoustic–flame interaction. The $b = 6$ eigenvalues are the most sensitive to a change in radius. The $b = 0$ eigenvalues, on the other hand, do not vary since they are independent of the gap radius size, as discussed in the previous section. All other eigenvalues lie, for any $\alpha > 0$, on the colored paths that connect the $b = 6$ with the $b = 0$ eigenvalues. Their distances along these paths from the $b = 0$ eigenvalues are larger the larger is b. In the limit $\alpha \to 0$, the $b \neq 0$ eigenvalues converge to the $b = 0$ eigenvalues. This leads to the formation of dense clusters of thermoacoustic eigenvalues with very close frequencies and growth rates for very small gap radii. The $b = 0$ thermoacoustic eigenvalue in Figure 7 (left) is unstable, which means that for very small radii ($\alpha < 2.5\%$), a whole cluster of thermoacoustic eigenvalues becomes unstable. This observation raises the question, how a whole cluster of linearly unstable eigenvalues with close frequencies and growth rates will interact in the nonlinear regime.

Analogous to the acoustic eigenvalues (see Figure 6), the thermoacoustic eigenvalues are observed to cluster more densely at higher frequencies; the difference in frequency between the

$b = 6$ and $b = 0$ thermoacoustic eigenvalues in Figure 7 (left) is 40 Hz, whereas in Figure 7 (right), a cluster with higher frequencies, the maximum distance between two thermoacoustic eigenvalues is only 25 Hz. Even though the acoustic–flame coupling can have a strong influence on the growth rates of thermoacoustic eigenvalues, this effect does not appear if the corresponding acoustic eigenvalues are very closely clustered, as it is the case for either small gap radii, or high frequencies. That small gap radii and high frequencies have analogous effects on the system eigenvalues could already be observed in Figure 4. In fact, either increasing the frequency to large values at a fixed value of α, or decreasing α at a fixed frequency, causes the effective reflection coefficients to converge to the sound hard limit, and leads to denser eigenvalue clustering.

Figure 8 shows the same acoustic and thermoacoustic eigenvalues as Figure 7 but for $\alpha = 30\%$. The black crosses mark the locations of flame eigenvalues, which correspond to the poles of the rational fit of the flame transfer function shown in Figure 3. In addition to thermoacoustic eigenvalues that converge to acoustic eigenvalues as the coupling is decreased ($m \to 0$), Figure 8 (left) shows another N eigenvalues that, instead, converge in this limit to a flame eigenvalue. Some thermoacoustic eigenvalues that converge to an acoustic eigenvalue for $\alpha = 5\%$, Figure 7 (left), converge for $\alpha = 30\%$ to flame eigenvalues. The location in the complex plane at which the eigenvalues change the nature of their origin is approximately the location of the $|b| = 2$ eigenvalues in Figure 8 (left)[1]. That thermoacoustic eigenvalues can converge to either acoustic or flame eigenvalues in the $m \to 0$ limit depending on a change in other parameters was discussed in more detail in [26]. The interaction of the two groups of thermoacoustic eigenvalues, one originating from acoustic, the other from flame eigenvalues, causes a strong dependence of the growth rates on a change in α, as recently discussed in [27, 26]. Some thermoacoustic eigenvalues change by more than 200 s^{-1} in growth rate[2] by a variation from $\alpha = 0$ to $\alpha = 30\%$.

In all other groups of thermoacoustic eigenvalues, no interaction with flame eigenvalues is observed and the eigenvalues qualitatively behave as the ones shown in Figure 8 (right) when α is varied. The change in α shifts the acoustic eigenvalues mostly in frequency and, due to the acoustic–flame coupling, the thermoacoustic eigenvalues in frequency and growth rate, as it was observed in Figure 7 for $\alpha = 5\%$. The shift in growth rate can cause thermoacoustic eigenvalues to be stable for some values of α and unstable for others.

Figure 9 shows the frequencies and growth rates of a thermoacoustic eigenvalue cluster, with eigenvalues between 0 and 100 Hz, as a function of α. It can be observed that the $b \neq 0$ eigenvalues grow out of the $b = 0$ eigenvalue, which leads to dense eigenvalue clustering for a weak acoustic coupling. As the $b = 0$ eigenvalue is not affected by a change in α, its growth rate and frequency are constant. Since all other eigenvalues travel along the same path for varying α, all of them reach the same minimum (maximum) growth rate at the same frequency, but for different values of α. The frequencies of the $b \neq 0$ thermoacoustic eigenvalues increase for increasing α and converge to the push–pull eigenvalue which converges to a constant value for large α. These results qualitatively agree with those presented for acoustic eigenvalues in [4], Figure 7, which shows the frequency of the eigenvalues for a varying geometric aspect ratio, can length over can cross-sectional area. If the increase in this aspect ratio is caused by a decrease in can radius, then its effect is comparable with an increase in α.

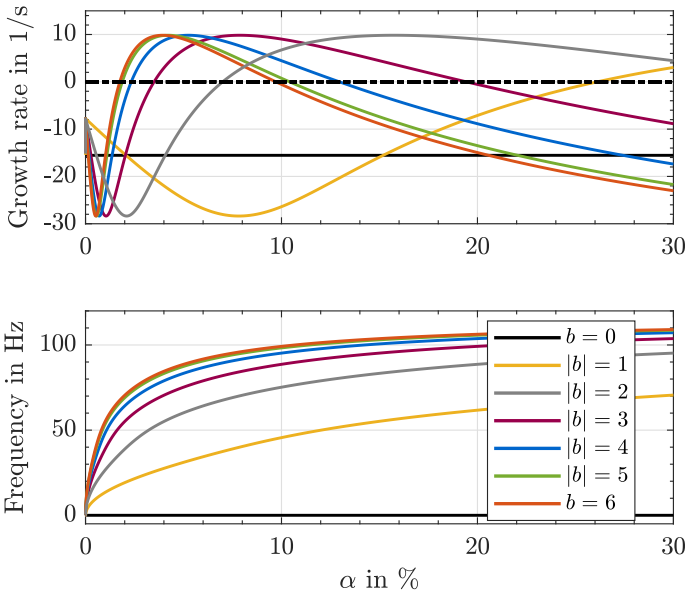

FIGURE 9: Frequencies and growth rates of an eigenvalue cluster with eigenvalues between 0 and 100 Hz, as a function of α. The color indicates the Bloch wavenumber.

For large values of α, the effective reflection coefficients for $b \neq 0$ are close to -1 for a relatively large range of frequencies. This is because the transition from $R_b = -1$ (open-end) to $R_b = +1$ (closed-end) is shifted to higher frequencies for larger α, as shown in Figure 4. Consequently, for increasing α, the effective reflection coefficients move towards the $R_b = -1$ limit and the eigenvalues for $b \neq 0$ move closer to the position of the eigenvalue that is found for an open-end boundary condition ($R_2 = -1$). The push–pull eigenvalue is the most sensitive to changes in α and reaches the limit first, followed by the eigenvalues with similar azimuthal orders. The lower limit ($R_b = -1$) of the effective reflection coefficient can cause eigenvalues with high azimuthal order to be very close in frequency and growth

[1] This is not a general feature. It is the particular complex frequency at which thermoacoustic eigenvalues of intrinsic and acoustic origin strongly interact for these specific two clusters.

[2] A factor of more than 20 compared to the baseline single-can growth rate of 10 s^{-1}.

rate for high values of α, as shown in Figure 9 and Figure 8 for the $|b| = 4, 5, 6$ eigenvalues. This demonstrates that dense eigenvalue clustering can also arise for a strong acoustic coupling and is not restricted to the weak-coupling case. However, for strong acoustic coupling, these dense clusters do not contain all the N eigenvalues associated with all possible Bloch wavenumbers b, as it is the case for weak acoustic coupling. The dense clustering for a strong coupling is restricted to groups of eigenvalues at low frequencies because the eigenvalues at high frequencies cluster close to the $b = 0$ (closed-end) eigenvalue, as discussed in the previous section. For eigenvalues at higher frequencies, α must be increased to very large values in order to reach the open-end limit, which cannot be considered within the present framework since the gaps are assumed to be acoustically compact.

Conclusions

In the present work, we introduced a low-order network model for thermoacoustic oscillations in a generic can-annular combustor. The model assumes plane acoustic waves inside the cans and a coupling boundary condition that is derived under the assumption of acoustically compact connection gaps between the cans at their downstream end. The coupling boundary condition is based on acoustic flux conservation and the Rayleigh conductivity. By exploiting the discrete rotational symmetry of the can-annular combustor, the coupling boundary condition can be expressed in form of an effective Bloch-type boundary condition. The Bloch formalism reduces the order of the model by the degree of symmetry of the system. Thus, only a single can with effective Bloch-type boundary condition needs to be considered in order to solve for eigenvalues of the generic can-annular combustor. The reduction of the order of the model reduces computational costs, even though the reduced-order model has to be solved for all independent Bloch wavenumbers to find all eigenvalues.

The strength of the coupling between the cans is described by means of the Rayleigh conductivity K_R. For the present study, we used a constant Rayleigh conductivity model, which scales with the connection gap radius for circular gaps, neglects the wall thickness between the gaps and mean flow effects. By neglecting the thickness of the walls, an additional frequency dependent time lag is omitted, which may be relevant when considering the acoustics of can-annular combustors. The presented generic can-annular model, nonetheless resolves the most important dynamical features of can-annular combustors, which have been reported in various studies. In order to represent more realistic acoustic coupling scenarios between the cans with less assumptions, more complex models of the Rayleigh conductivity could be considered.

We analyzed the frequency response of the Bloch-type boundary condition in form of an effective reflection coefficient and used the Bloch ansatz and the effective reflection coefficient to analyze how acoustic waves are transmitted from one can into the others, as a function of their distance. Results are qualitatively in good agreement with results from a two dimensional study, which resolves the acoustic near field effects around the gaps [4].

We then used the effective boundary condition to construct a low-order (thermo)acoustic network model of a generic $N = 12$ can-annular combustor. When no unsteady heat release is considered, acoustic eigenvalues are observed to form clusters with close frequencies and growth rates. The clustering of acoustic eigenvalues was found to be stronger for groups of eigenvalues at higher frequencies.

By varying the connection gap radius, we investigate the effect of coupling strength on the location of acoustic and thermoacoustic eigenvalues of the generic can-annular combustor model. The eigenvalues are more sensitive to a change of coupling strength the higher the Bloch wavenumber is. Acoustic eigenvalues within a cluster are mostly shifted in frequency, whereas thermoacoustic eigenvalues show also a strong sensitivity in growth rate. As the coupling strength is increased, starting from the closed-end limit, the eigenvalues for $b \neq 0$ grow out of the $b = 0$ eigenvalues. This results in dense clusters of eigenvalues with very close frequency and growth rate for weak can-to-can coupling. It implies that, if the cans of a can-annular system are designed in such a way that their eigenvalues have negative growth rates for a closed end boundary condition, the eigenvalues of the corresponding can-annular system will also have negative growth rates, for a weak acoustic coupling between the cans. On the other hand, if an eigenvalue of the single-can system is unstable, the corresponding can-annular system will, for a weak acoustic coupling, show a whole set of linearly unstable eigenvalues.

We demonstrated that also for a strong acoustic can-to-can coupling, eigenvalues at low frequencies and for large Bloch wavenumbers can form dense clusters of eigenvalues, with very close frequencies and growth rates, close to the eigenvalues that are found for a corresponding system with an open-end boundary condition. The formation of eigenvalue clusters raises the question how a set of modes with close frequency and growth rate but, as each eigenvalue corresponds to a different azimuthal order, with very different mode shapes, will interact in the nonlinear regime and which oscillation pattern(s) will be observed.

Acknowledgments

Jakob von Saldern thanks the ERASMUS+ program and the Studienstiftung des Deutschen Volkes for financial support. Alessandro Orchini is grateful to the DFG (Project Nr. 422037803) for funding his position as PI.

A Low-frequency response of transmission coefficients

From Eq. (15), for $k \neq 0$ we have

$$\lim_{i\omega\to 0}|T_k| = \lim_{i\omega\to 0}\left|\frac{1}{N}\sum_{b=0}^{N} R_b(s)e^{-ib(\theta_k)}\right| = \ldots$$
$$\left|\frac{1}{N}(1-\sum_{b\neq 0} e^{-ib(\theta_k)})\right| = \left|\frac{1}{N}(1-\sum_{b\neq 0}\cos(b\theta_k) - i\sin(b\theta_k))\right|. \tag{18}$$

The imaginary part is zero since the sin-function is odd and $\theta_k = (k2\pi/N)$. Note that any N consecutive Bloch wavenumbers can be considered. The sum over the $\cos(b\theta_k)$ yields -1:

$$\sum_{b=1}^{N-1}\cos(b\theta_k) = Re\left[\sum_{b=1}^{N-1} e^{ib\theta_k}\right] = \ldots$$
$$Re\left[e^{i\theta_k}\frac{e^{i(N-1)\theta_k}-1}{e^{i\theta_k}-1}\right] = \frac{\sin((N-1)k\pi/N)}{\sin(k\pi/N)}\cos(k\pi)\ldots \tag{19}$$
$$= -\cos(k\pi)^2 = -1.$$

The relation between the first and second lines of Eq. (19) is based on the known result for the geometric series

$$\sum_{b=1}^{N} e^{ib\theta_k} = e^{i\theta_k}\frac{e^{iN\theta_k}-1}{e^{i\theta_k}-1}. \tag{20}$$

REFERENCES

[1] Kaufmann, P., Krebs, W., Valdes, R., and Wever, U., 2008. "3d thermoacoustic properties of single can and multi can combustor configurations". In ASME Turbo Expo, pp. 527–538.

[2] Panek, L., Huth, M., and Farisco, F., 2017. "Thermoacoustic characterization of can-can interaction of a can-annular combustion system based on unsteady cfd les simulation". In First Global Power and Propulsion Forum, Zurich, Switzerland, Jan, pp. 16–18.

[3] Farisco, F., Panek, L., and Kok, J. B., 2017. "Thermoacoustic cross-talk between cans in a can-annular combustor". *International Journal of Spray and Combustion Dynamics,* ***9***, pp. 452–469.

[4] Ghirardo, G., Di Giovine, C., Moeck, J. P., and Bothien, M. R., 2018. "Thermoacoustics of Can-Annular Combustors". *Journal of Engineering for Gas Turbines and Power,* ***141***, p. 011007.

[5] Moon, K., Jegal, H., Gu, J., and Kim, K. T., 2019. "Combustion-acoustic interactions through cross-talk area between adjacent model gas turbine combustors". *Combustion and Flame,* ***202***, pp. 405 – 416.

[6] Jegal, H., Moon, K., Gu, J., Li, L. K., and Kim, K. T., 2019. "Mutual synchronization of two lean-premixed gas turbine combustors: Phase locking and amplitude death". *Combustion and Flame,* ***206***, pp. 424–437.

[7] Dowling, A. P., and Stow, S. R., 2003. "Acoustic analysis of gas turbine combustors". *Journal of Propulsion and Power,* ***19***, pp. 751–764.

[8] Bauerheim, M., Parmentier, J.-F., Salas, P., Nicoud, F., and Poinsot, T., 2014. "An analytical model for azimuthal thermoacoustic modes in an annular chamber fed by an annular plenum". *Combustion and Flame,* ***161***, pp. 1374–1389.

[9] Rayleigh, J. W. S., 1945. *The theory of sound, Vol. 2*. Dover.

[10] Howe, M., 1979. "On the theory of unsteady high Reynolds number flow through a circular aperture". *Proceedings of the Royal Society of London. A. Mathematical and Physical Sciences,* ***366***, pp. 205–223.

[11] Luong, T., Howe, M., and McGowan, R., 2005. "On the Rayleigh conductivity of a bias-flow aperture". *Journal of Fluids and Structures,* ***21***, pp. 769–778.

[12] Howe, M., Scott, M., and Sipcic, S., 1996. "The influence of tangential mean flow on the Rayleigh conductivity of an aperture". *Proceedings of the Royal Society of London. Series A: Mathematical, Physical and Engineering Sciences,* ***452***, pp. 2303–2317.

[13] Grace, S., Howe, M., and Horan, K., 1997. "The influence of grazing flow on the Rayleigh conductivity of an aperture of arbitrary shape". In 3rd AIAA/CEAS Aeroacoustics Conference, p. 1672.

[14] Mensah, G. A., Campa, G., and Moeck, J. P., 2016. "Efficient Computation of Thermoacoustic Modes in Industrial Annular Combustion Chambers Based on Bloch-Wave Theory". *Journal of Engineering for Gas Turbines and Power,* ***138***, p. 081502.

[15] Bloch, F., 1929. "Über die Quantenmechanik der Elektronen in Kristallgittern". *Zeitschrift für Physik,* ***52***, pp. 555–600.

[16] McManus, K., Poinsot, T., and Candel, S. M., 1993. "A review of active control of combustion instabilities". *Progress in Energy and Combustion Science,* ***19***, pp. 1–29.

[17] Dowling, A. P., 1995. "The calculation of thermoacoustic oscillations". *Journal of Sound and Vibration,* ***180***, pp. 557–581.

[18] Polifke, W., 2010. "Low-Order Analysis Tools for Aero- and Low-Order Analysis Tools for Aero- and Thermo-Acoustic Instabilities". In Lecture Series "Advances in Aero-Acoustics and Thermo-Acoustics", Von Karman Institute.

[19] Dowling, A. P., 1999. "A kinematic model of a ducted flame". *Journal of Fluid Mechanics,* ***394***, pp. 51–72.

[20] Schuller, T., Ducruix, S., Durox, D., and Candel, S., 2002. "Modeling tools for the prediction of premixed flame transfer functions". *Proceedings of the Combustion Institute,* ***29***, pp. 107–113.

[21] Lieuwen, T., 2003. "Modeling premixed combustion–acoustic wave interactions: A review". *Journal of Propulsion and Power,* ***19***, pp. 765–781.

[22] Kashinath, K., Hemchandra, S., and Juniper, M. P., 2013. "Nonlinear phenomena in thermoacoustic systems with premixed flames". *Journal of Engineering for Gas Turbines and Power,* ***135***, p. 061502.

[23] Orchini, A., Illingworth, S. J., and Juniper, M. P., 2015. "Frequency domain and time domain analysis of thermoacoustic oscillations with wave-based acoustics". *Journal of Fluid Mechanics,* ***775***, pp. 387–414.

[24] Semlitsch, B., Orchini, A., Dowling, A. P., and Juniper, M. P., 2017. "G-equation modelling of thermoacoustic oscillations of partially premixed flames". *International Journal of Spray and Combustion Dynamics,* ***9***, pp. 260–276.

[25] Gustavsen, B., and Semlyen, A., 1999. "Rational approximation of frequency domain responses by vector fitting". *IEEE Transactions on Power Delivery,* ***14***, pp. 1052–1061.

[26] Orchini, A., Silva, C. F., Mensah, G. A., and Moeck, J. P., 2020. "Thermoacoustic modes of intrinsic and acoustic origin and their interplay with exceptional points". *Combustion and Flame,* ***211***, pp. 83–95.

[27] Sogaro, F. M., Schmid, P. J., and Morgans, A. S., 2019. "Thermoacoustic interplay between intrinsic thermoacoustic and acoustic modes: non-normality and high sensitivities". *Journal of Fluid Mechanics,* ***878***, pp. 190–220.